

Thrust generation by a heaving flexible foil: Resonance, nonlinearities, and optimality

Florine Paraz, Lionel Schouveiler, and Christophe Eloy^{a)}

*Aix Marseille Université, CNRS, Centrale Marseille, IRPHE UMR 7342,
13013 Marseille, France*

(Dated: 16 November 2015)

Flexibility of marine animal fins has been thought to enhance swimming performance. However, despite numerous experimental and numerical studies on flapping flexible foils, there is still no clear understanding of the effect of flexibility and flapping amplitude on thrust generation and swimming efficiency. Here, to address this question, we combine experiments on a model system and a weakly nonlinear analysis. Experiments consist in immersing a flexible rectangular plate in a uniform flow and forcing this plate into a heaving motion at its leading edge. A complementary theoretical model is developed assuming a two-dimensional inviscid problem. In this model, nonlinear effects are taken into account by considering a transverse resistive drag. Under these hypotheses, a modal decomposition of the system motion allows us to predict the plate response amplitude and the generated thrust, as a function of the forcing amplitude and frequency. We show that this model can correctly predict the experimental data on plate kinematic response and thrust generation, as well as other data found in the literature. We also discuss the question of efficiency in the context of bio-inspired propulsion. Using the proposed model, we show that the optimal propeller for a given thrust and a given swimming speed is achieved when the actuating frequency is tuned to a resonance of the system, and when the optimal forcing amplitude scales as the square root of the required thrust.

I. INTRODUCTION

Aquatic vertebrates can either use their caudal fin or their median and paired fins for propulsion¹. Generally, these appendages are flexible²⁻⁴, and it has often been argued that flexibility enhances swimming efficiency⁵⁻⁷. Yet, the rigidity of caudal fins can vary substantially between species: tuna have relatively rigid caudal fins^{1,8} compared to goldfish² or trouts⁹. To date, it remains to be proven whether or not fin flexibility is an evolutionary advantage.

Swimming kinematics has been first explored through experimental observations of live fish¹⁰⁻¹². These experiments have revealed that most fish and cetacean species use a particular mode of locomotion, called undulatory swimming, which consists in bending the backbone to generate a propagative wave from head to tail. Some species like sharks and tuna use an extreme form of undulatory swimming, a thunniform mode^{13,14}, where significant values of the curvature are located in the caudal peduncle region only. For these animals, the anterior part of the body is almost rigid and can be considered as a cargo, while the posterior flexible part (made of the caudal peduncle and caudal fin) can be considered as a propeller. Such systems have obvious engineering applications to the design of novel bio-inspired propellers¹⁵ and led to specific studies on oscillating *rigid* foils¹⁶⁻¹⁸. In agreement with a two-dimensional, linear, and inviscid theory on

^{a)}christophe.eloy@irphe.univ-mrs.fr

oscillating wings^{19–21}, it has been found experimentally that a combination of heave and pitch with a phase difference of 90° corresponds to an optimum for propulsion^{22,23}. For these two-dimensional rigid foils, it was also found experimentally¹⁸ that the optimal frequency corresponds to a Strouhal number $St \approx 0.3$ ($St = fA/U$, with f the oscillating frequency, A the peak-to-peak amplitude of the trailing edge motion, and U the swimming velocity). Since the Strouhal numbers of many aquatic species have been measured in the interval $0.2 < St < 0.4$, some authors claimed that this interval corresponds to optimal performance^{17,24}. However the link between Strouhal number and optimality is still debated today²⁵.

Recently, these studies on oscillating rigid foils of large aspect ratio have been extended to *flexible* foils. Experiments on such flexible foils have been performed with pitching motions^{26,27}, heaving motions^{6,7,28–31} or a combination of both motions^{32,33}. For all cases, it was shown that a resonance phenomenon occurs: thrust generation is maximal at the natural frequencies of the system. In other words, when the system fluid+structure is forced at one of its eigenfrequencies, the response in terms of elastic deformation is maximized, and thrust generation and performance have also been reported to be maximized.

Numerical simulations of a flapping flexible appendage have been conducted, either in the limit of infinite Reynolds number using vortex methods^{5,29,34}, or at small to moderate Reynolds numbers using direct numerical simulations^{35–39}. Similarly to experiments, these simulations generally showed a connection between the resonance of the fluid+structure system and the generated thrust. There is thus a strong contrast between rigid and flexible foils: in the rigid case, optimal frequency is determined by a specific value of the Strouhal number^{17,24}; in the flexible case, optimal frequency is a natural frequency of the deformable system. Interestingly, since the Strouhal number varies linearly with amplitude while natural frequencies are almost independent on amplitude, these two frequencies can be matched by adjusting the flapping amplitude²⁶. But, to assess if this particular amplitude corresponds to an overall optimum, one has to systematically study the effect of the forcing amplitude on thrust production, a study that has rarely been performed³¹.

Although thrust production by a flexible foil has been studied many times both experimentally and numerically, there have been comparatively few attempts to address this problem analytically. Among these attempts, Moore⁴⁰ recently extended the works of Wu^{19,21} and Lighthill²⁰ on the optimization of oscillating foils. He modeled a two-dimensional rigid foil whose leading edge is forced into a heaving motion and which can passively pitch. In agreement with experiments and numerical simulations, he found that driving the foil near a resonance can dramatically increase the swimming performances. Some of us also used Wu’s and Lighthill’s ideas to model the thrust produced by an active flexible foil⁴¹, and this analytic model was used to calculate the optimal two-dimensional swimming gait of a self-propelled foil. Finally, Alben *et al.*²⁹ used a linear time-harmonic model to rationalize the power-law scalings observed in their numerical simulations. However, these analytical studies are mainly linear and are thus limited to motions of small amplitude. One objective of the present study is to extend these modeling approaches to take into account nonlinearities.

The organization of the paper is as follows. Section II introduces the experimental setup, and Sec. III describes the weakly nonlinear model. Then, the results obtained with both approaches are presented and compared, in Sec. IV, through the kinematic response of the system, the wake, the production of thrust, and the efficiency of the propulsion system. Finally, these results are discussed in the context of biological and bio-inspired swimming in Sec. V.

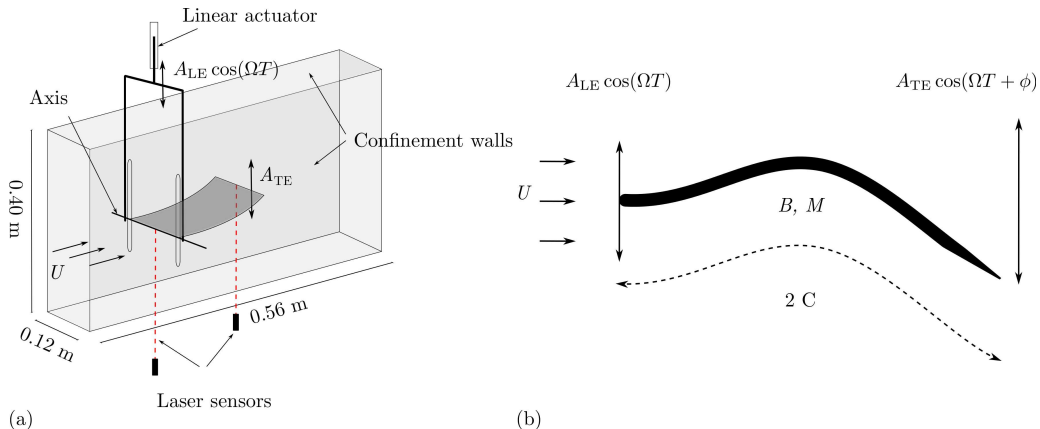


FIG. 1. (a) Experimental set-up and (b) two-dimensional modeling.

II. EXPERIMENTAL METHODS

The experimental set-up consists of a flexible foil with a rounded leading edge and a tapered trailing edge. This foil (hereinafter called foil or plate indifferently) of bending rigidity B is immersed in a uniform flow of speed U (Fig. 1). It is made of polysiloxane and has an aspect ratio $S/C = 1$, where $S = 6$ cm and $C = 6$ cm are its half-span and half-chord. Flapping is achieved by heaving harmonically the foil leading edge through an inverted U-frame, with a heave amplitude a_{LE} and angular frequency Ω .

The foil is isolated from the guiding rods and the free surface by two vertical and one horizontal transparent confinement walls. The foil is clamped into the actuated rod to ensure that its leading edge always remains parallel to the incoming flow. The foil density being approximately 20% heavier than water, its deformation can be slightly asymmetric in some experimental cases.

The plate deflection at the leading and trailing edges is measured with two laser sensors Keyence G-402, while its full deformation is recorded by a video camera through a side wall. The thrust is measured with two load cells Futek LSB210 assembled parallel to the flow at the leading edge. In addition, a particle image velocimetry (PIV) system is used to measure the wake beyond the trailing edge. The PIV acquisition system is composed of two pulsed YAG lasers and a high precision camera (1336×2000 pixels). PIV velocity fields are computed using the software DPIVSoft⁴².

In this experimental set-up, four parameters can be varied: the bending rigidity B , the flow speed U , the forcing angular frequency Ω , and the forcing amplitude A_{LE} . Table I specifies the range of these parameters. To vary the bending rigidity, we use three foils made of different polysiloxane formulae. Their rigidities are deduced from their first natural frequency Ω_0 , which are measured from an impulse response test in water (Fig. 2). We find that the natural frequencies of the system foil+fluid are $\Omega_0 = 4.71, 6.22,$ and 8.17 rad s^{-1} , corresponding to bending rigidities per unit span $B = 19.6MC^4\Omega_0^2 = 0.027, 0.047,$ and 0.081 N m respectively (see Sec. IV A for details on this calculation).

As it can be seen in Fig. 2, impulse response tests in water yield strongly damped oscillations. This damping can be decomposed into three components: internal viscoelastic damping, linear fluid damping, and nonlinear fluid damping. From these impulse response tests, together with additional tests performed in air, these sources of damping can be quantified and included in a model (Appendix B).

A typical experiment consists in a frequency response test: for a plate of given bending rigidity, the flow speed U and forcing amplitude A_{LE} are fixed, and the plate response is recorded as the forcing frequency Ω is gradually varied. Experiments are then repeated

TABLE I. Characteristic parameters of the experiment.

	Symbols	Values	Units
Forcing amplitude	A_{LE}	0.004 – 0.014	m
Forcing frequency	Ω	2.51 – 37.70	rad s ⁻¹
Bending rigidity (per unit span)	B	0.027 – 0.081	Nm
Fluid speed	U	0 – 10.10 ⁻²	m s ⁻¹
Foil half-chord	C	0.06	m
Foil half-span	S	0.06	m
Foil surface density	M	4.8	kg m ⁻²
Fluid density	ρ	10 ³	kg m ⁻³

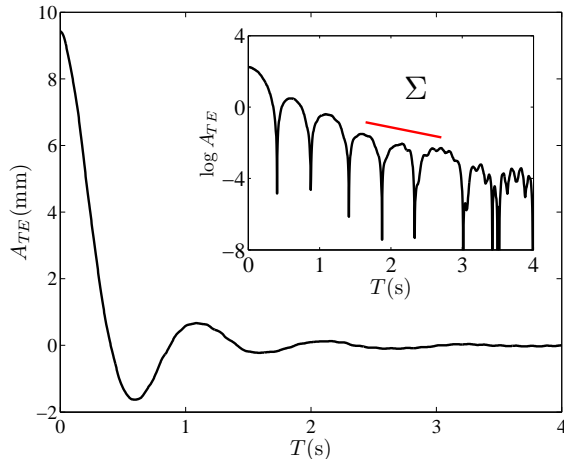


FIG. 2. The impulse response of the most flexible foil in water. A fast Fourier transform of the signal gives the natural frequency Ω_0 and (*inset*) the slope of the signal in semilogarithmic scale gives the damping coefficient Σ .

for different amplitudes A_{LE} , different flow speeds U , and using plates of different bending rigidity B to assess the effect of these control parameters³¹.

III. ANALYTICAL MODEL

A. Governing equation

The system is made dimensionless by using C , $C^2\sqrt{M/B}$ and $\rho B/MC^2$ as characteristic length, time and pressure respectively, with C the plate half-chord, B its bending rigidity, M its mass per unit area, and ρ the fluid density (Table I). Using lowercase letters to denote dimensionless variables, the system we want to model can be represented as a flexible foil of infinite span, zero thickness, half-chord unity, immersed in a uniform flow along the x -axis of speed $u = UC\sqrt{M/B}$ (Fig. 3).

At the leading edge ($x = -1$), the foil is clamped and forced into a harmonic heave motion, $a_{LE} \cos(\omega t)$, while the rest of the foil responds elastically with a deflection $h(x, t)$. The dimensionless frequency, $\omega = \Omega C^2\sqrt{M/B}$, corresponds to the ratio of the forcing frequency to a typical elastic frequency. In this problem, another dimensionless frequency can be built, the reduced frequency $k = \Omega C/U = \omega/u$, which is the ratio between the forcing frequency and a “fluid” frequency calculated as the inverse of the time taken by

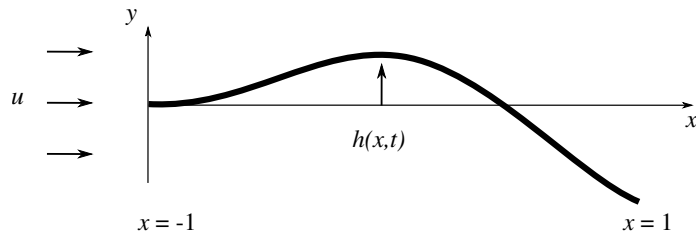


FIG. 3. Sketch of the problem.

fluid particles to travel one half-chord at speed U . In this section, we will assume that k is asymptotically large (i.e. $\omega \gg u$), in conformity with the range of parameters explored in the present experiments (Table I).

We assume that the plate deflection follows a linearized Euler–Bernoulli beam equation

$$\partial_t^2 h + \partial_x^4 h + \nu \partial_t h + \mu \partial_t \partial_x^4 h + \frac{c_D}{2m} |\partial_t h| \partial_t h + \frac{p}{m} = 0, \quad (1)$$

complemented with clamped-free boundary conditions: $h(-1, t) = a_{\text{LE}} \cos(\omega t)$ and $\partial_x h(-1, t) = \partial_x^2 h(1, t) = \partial_x^3 h(1, t) = 0$. In the equation of motion (1), the first two terms represent the equation of an elastic beam in vacuum (inertia and elastic restoring force respectively), the next two terms represent the linear damping in the system (linear fluid damping and internal viscoelastic damping, see Appendix B), the fifth term describes the nonlinear fluid damping (which takes the form of a transverse drag force with drag coefficient c_D), and the last term corresponds to the pressure forces on the plate with p the pressure jump across the beam.

In the above equation of motion, the damping coefficients ν and μ , are determined independently from linear impulse response tests (Appendix B). The ratio $m = M/\rho C$ is small in the present case because the plate thickness is small compared to its chord and the material has a density close to water.

Assuming that the deflection is small (i.e. $h \ll 1$ and $\partial_x h \ll 1$), the pressure jump across the foil p can be calculated using unsteady airfoil theory. This calculation is based on the work of Wu^{19,21} with the simplifying assumption that the reduced frequency $k = \omega/u$ is asymptotically large (Appendix A). Note that in Wu’s approach, the velocity induced by the plate motion is implicitly assumed to be small compared to the uniform flow velocity, i.e. $\omega a_{\text{LE}} \ll u$ or $a_{\text{LE}} \ll k^{-1}$. This is an important restriction on the amplitudes a_{LE} that can be considered valid. Unfortunately, in most experimental cases considered in this study, this assumption is not fulfilled. Yet, as it will be shown below, we find a good agreement between theory and experiments.

Within this framework, the flow is assumed to be potential except in a thin wake located at $y = 0$ for $x > 1$. This wake is due to vortex shedding at the trailing edge and ensures the continuity of pressure through a Kutta condition⁴³. However, an inverse square root pressure singularity remains at the leading edge due to a non zero angle of attack. This singularity smooths out if the finite thickness of the foil is accounted for, but causes leading edge suction, a force along the x -direction that participates in the thrust produced. As we shall see below, this force, also called suction force, is of crucial importance.

TABLE II. Values of the coefficients κ_i , α_i and β_{ij} of Eq. (4) for the first three beam eigenmodes.

	i=1	i=2	i=3
κ_i	0.938	2.347	3.927
α_i	0.783	0.434	0.254
β_{i0}	1.188	1.015	0.288
β_{i1}	1.131	0.591	-0.014
β_{i2}	0.591	1.004	0.251
β_{i3}	-0.014	0.251	0.556

B. Modal analysis

To solve equation of motion (1), the deflection is decomposed as

$$h(x, t) = \left(a_{\text{LE}} + \sum_{i=1}^N a_i h_i(x) \right) e^{i\omega t}, \quad (2)$$

where we have neglected higher time harmonics. It represents a combination of the imposed displacement of amplitude a_{LE} , and N eigenmodes $h_i(x)$ of a beam in vacuum of complex amplitudes a_i (cf. Appendix A). In practice, we will use $N = 3$, which is enough to represent the foil deflection around the first two resonances. The eigenmodes $h_i(x)$ have the property of being an orthonormal basis of the clamped-free deflections when the following scalar product is used

$$\langle f, g \rangle = \frac{1}{2} \int_{-1}^1 f(x)g(x)dx. \quad (3)$$

Inserting the decomposition (2) into (1) and forming the scalar product with the N eigenmodes $h_i(x)$ yields N nonlinearly coupled equations for the N unknown amplitudes a_i of the form

$$\begin{aligned} & (i\omega\nu - \omega^2)(\alpha_i a_{\text{LE}} + a_i) + (1 + i\omega\mu)\kappa_i^4 a_i \\ & + i\omega^2 \frac{c_D}{m} \frac{2}{3\pi} \int_{-1}^1 h_i \left| a_{\text{LE}} + \sum_{j=1}^N a_j h_j(x) \right| \left(a_{\text{LE}} + \sum_{j=1}^N a_j h_j(x) \right) dx \\ & - \frac{\omega^2}{m} \left(\beta_{i0} a_{\text{LE}} + \sum_{j=1}^N \beta_{ij} a_j \right) = 0, \quad (4) \end{aligned}$$

for $1 \leq i \leq N$. The coefficients α_i and β_{ij} , whose expressions are given in Appendix A, are universal and have been calculated (Table II). In the system (4), we recognize the same terms as in Eq. (1): the first term gathers linear fluid damping and inertia, the second term gathers elasticity and viscoelasticity, the third term is the nonlinear damping, and the last term is due to the pressure forces. In the limit of large reduced frequency, $\omega \gg u$, this last term is proportional to ω^2 and therefore plays the role of an added mass. As it can be seen in (4), the different eigenmodes are only coupled through the pressure term and through the nonlinear damping term. Equation (4) represents a weakly nonlinear model, correct up to the order $O(a_{\text{LE}}^2)$. To develop an analytical model correct up to the order $O(a_{\text{LE}}^3)$, geometrical nonlinearities would have to be taken into account, making the problem far more complex⁴⁴.

The system (4) for $1 \leq i \leq N$ can be solved numerically for any values of the forcing amplitude a_{LE} and forcing frequency ω . Its solution gives the complex amplitudes a_i as

a function of the parameters a_{LE} and ω (e.g., Fig. 6). In particular it gives the amplitude a_{TE} and phase ϕ of the trailing edge oscillation relative to the leading edge forcing

$$h(1, t) = \left(a_{\text{LE}} + \sum_{i=1}^N a_i h_i(1) \right) e^{i\omega t} = a_{\text{TE}} e^{i(\omega t + \phi)}. \quad (5)$$

IV. RESULTS

A. Resonance

We now examine the frequency response of the system, both experimentally and theoretically. In dimensionless units, it consists in measuring the relative amplitude of the trailing edge displacement $a_{\text{TE}}/a_{\text{LE}}$ and its phase ϕ , when the normalized forcing frequency ω/ω_0 is varied. Here ω_0 is the first natural frequency of the foil+fluid system. It is determined through impulse responses tests in the experiments (Sec. II) and given by $\omega_0 = \kappa_1^2 / \sqrt{1 + \beta_{11}/m} \approx 0.226$ for the model [this formula results from taking $a_{\text{LE}} = a_2 = a_3 = 0$ in Eq. (4) and neglecting nonlinear terms]. Given the range of control parameters (Table I), the system is investigated in the limit of small reduced mass and large reduced frequency ($m \ll 1$ and $k \gg 1$). In this limit, we have shown in a previous paper³¹ that the frequency response depends mainly on the forcing amplitude imposed at the leading edge a_{LE} . In other words, the fluid speed and the plate bending rigidity have little influence on the response as long as deflection amplitudes and frequencies are made dimensionless properly.

Figure 4 shows three frequency responses for different forcing amplitudes. Both experiments (symbols) and theoretical predictions (solid lines) exhibit two resonant peaks in the range of frequencies explored (Fig. 4a). Here, the only fitting parameter is the drag coefficient c_D : the value $c_D = 12$ has been found by fitting the experimental value of the first peak amplitude for the intermediate forcing amplitude $a_{\text{LE}} = 0.17$. This value appears much larger than the value $c_D \approx 2$ usually reported in the literature for a rigid⁴⁵ or flexible plate^{46,47}. This unexpected high value of c_D could result from other nonlinear contributions that arise in the problem, such as the rotational drag⁴⁸ or the nonlinear terms of order $O(a_{\text{LE}}^3)$ and higher that have been neglected. The use of an “effective drag” gathering all nonlinearities in a single term is validated by the agreement between experiments and theory for the two other forcing amplitudes $a_{\text{LE}} = 0.07$ and 0.24 (Fig. 4). In particular, the first resonant peak around $\omega/\omega_0 = 1$ is well predicted by the model, both in terms of frequency and amplitude.

It should be emphasized that the differences in relative amplitude $a_{\text{TE}}/a_{\text{LE}}$ for different forcing amplitudes a_{LE} are a signature of nonlinear effects (Fig. 4a). A linear model would give the same relative response for any forcing amplitude (Fig. 4c).

For the second resonant peak in Fig. 4a, the agreement between experiments and theory is good, except for the largest forcing $a_{\text{LE}} = 0.24$. However, phase differences tend to be underestimated (Fig. 4b), maybe because nonlinear effects of order $O(a_{\text{LE}}^3)$ and higher have been neglected in the analysis.

To go further in the comparison between experiments and theory, we now examine the plate deflection at the two resonances (Fig. 5). The envelope of the first resonant mode (Fig. 5a,b) is well captured by the model. It actually corresponds to a superposition of a rigid oscillation and a contribution of the first beam eigenmode (Fig. 6). For the second resonant mode, agreement is good, but some differences can be observed (Fig. 5c,d): in the experiments, there is a bulge at about 1/3 of the plate chord that is not visible in the model, and the neck at about 2/3 is less marked than in the prediction.

The kinematic response of the foil under an external forcing has now been characterized, but a central question remains: how do the nonlinear forces affect thrust production?

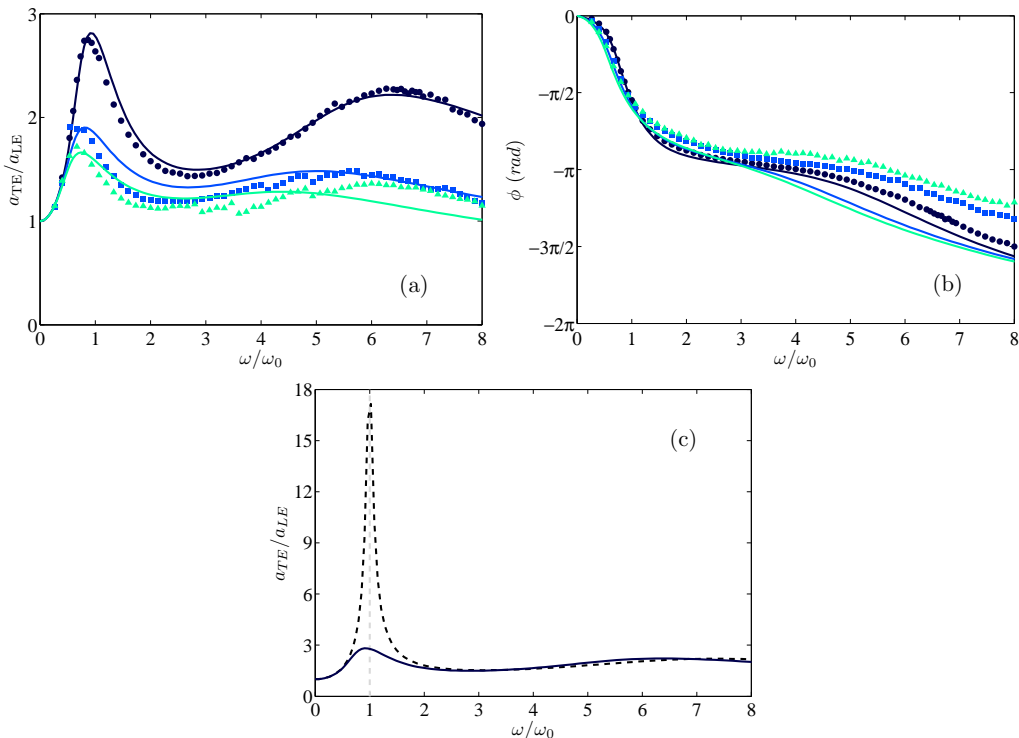


FIG. 4. Response of the trailing edge as a function of the forcing frequency ω/ω_0 : (a) relative amplitude a_{TE}/a_{LE} , (b) corresponding phase shift ϕ . Plate bending rigidity is $B = 0.027$ Nm and flow speed is zero. Symbols represent the experimental results while solid lines represent theoretical predictions for $c_D = 12$. Dark blue, medium blue, and light green correspond to the forcing amplitudes: $a_{LE} = 0.07, 0.17,$ and 0.24 respectively. (c) Theoretical trailing edge amplitude when nonlinear terms are neglected, i.e. $c_D = 0$ or a_{LE} asymptotically small (dashed line). For comparison purposes, the nonlinear result for $a_{LE} = 0.07$ is also shown (solid line, similar as dark blue solid line in a).

B. Thrust

If the flapping flexible foil generates a thrust, one expects a reverse Bénard-von Kármán vortex street in its wake⁴⁹; well-known to be a characteristic of a propulsive regime⁵⁰. Figure 7 shows phase-averaged PIV vorticity fields when the frequency is tuned to the first resonance. These fields confirm that a reverse Bénard-von Kármán vortex street is indeed present.

To quantify the thrust production from PIV velocity fields, one can plot the time-average of the x -component of the flow velocity u_x (Fig. 7). It shows that, on average, a jet is produced behind the heaving foil, with a maximum speed of about twice the imposed flow in this particular example. From a momentum balance argument, it can be shown⁵¹ that the thrust is given by

$$f_T = u \int_{-\infty}^{\infty} (u - u_x(x, y)) dy. \quad (6)$$

This dimensionless thrust is related to the dimensional thrust force per unit span by $F_T = \rho B f_T / MC$. A priori, for a two-dimensional problem, this momentum balance could be applied at any distance x far enough from the trailing edge. In practice an optimal distance x_{optim} should be chosen, which results from a compromise between a

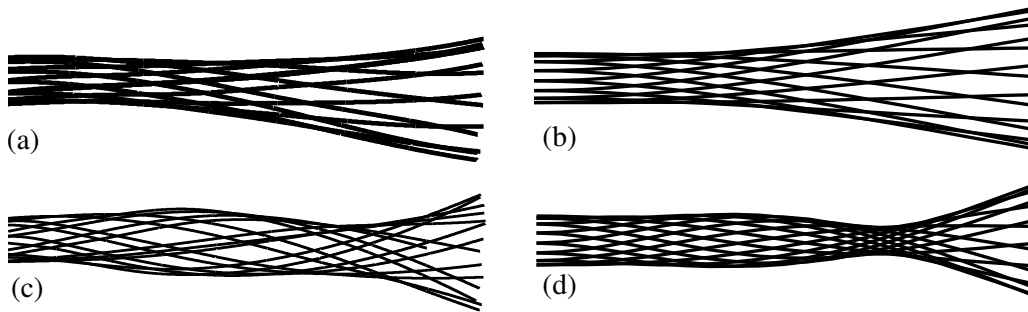


FIG. 5. Comparison between the experimental (a, c) and theoretical (b, d) deflection envelopes. These images show superimposed images of the foil over one heaving period. Deformation at the first resonance for $\omega/\omega_0 = 0.9$ (a,b) and the second resonance, which appears experimentally at $\omega/\omega_0 = 6.4$ (c) and theoretically at $\omega/\omega_0 = 5.8$ (d). These responses correspond to the dark blue data in Fig. 4, for $a_{LE} = 0.07$. Note that the asymmetry of the experimental deflections is due to the foil density that is 20% heavier than water. Note also that the first 4% of the plate near the leading edge are hidden by the U-frame and thus not shown here (a,c).

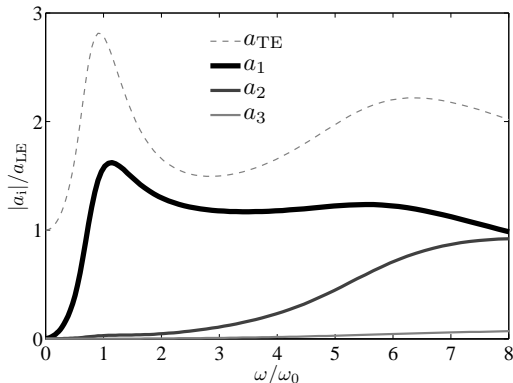


FIG. 6. Contribution of the amplitude a_1 , a_2 and a_3 in the total amplitude a_{TE} for $a_{LE} = 0.07$.

distance large enough so the pressure variations across the wake are weak, and small enough so the three-dimensional effects have not established yet⁵⁰. In our case, it has been found that $x_{\text{optim.}} \approx 3$ is appropriate (Fig. 7f). However, this method is only a raw approximation of the generated thrust, as three-dimensional and confinement effects are important in the set-up used here.

To calculate the thrust produced by the heaving foil from the weakly nonlinear model, we have to consider three contributions: the reactive forces per unit span, f_P , due to the pressure forces projected onto the x -direction²¹; the resistive forces, f_R , which are due to the nonlinear damping forces on the foil; and the leading-edge suction, f_S .

Leading-edge suction corresponds to large negative values of the pressure near the leading edge. However, the existence of important negative pressures can yield a stall vortex or a leading-edge vortex^{52,53}, whose shedding can strongly affect the flow and the suction force. In practice, when the angle of attack (i.e. the angle between the relative flow velocity and the plate) is too large, the suction force evaluated using linear theory cannot be achieved¹⁸. Here, the maximal value of the angle of attack, which is given by $\arctan(ka_{LE})$, is always larger than 15° , such that leading-edge suction can be neglected (when considering optimisation in the next section, this assumption will be lifted).

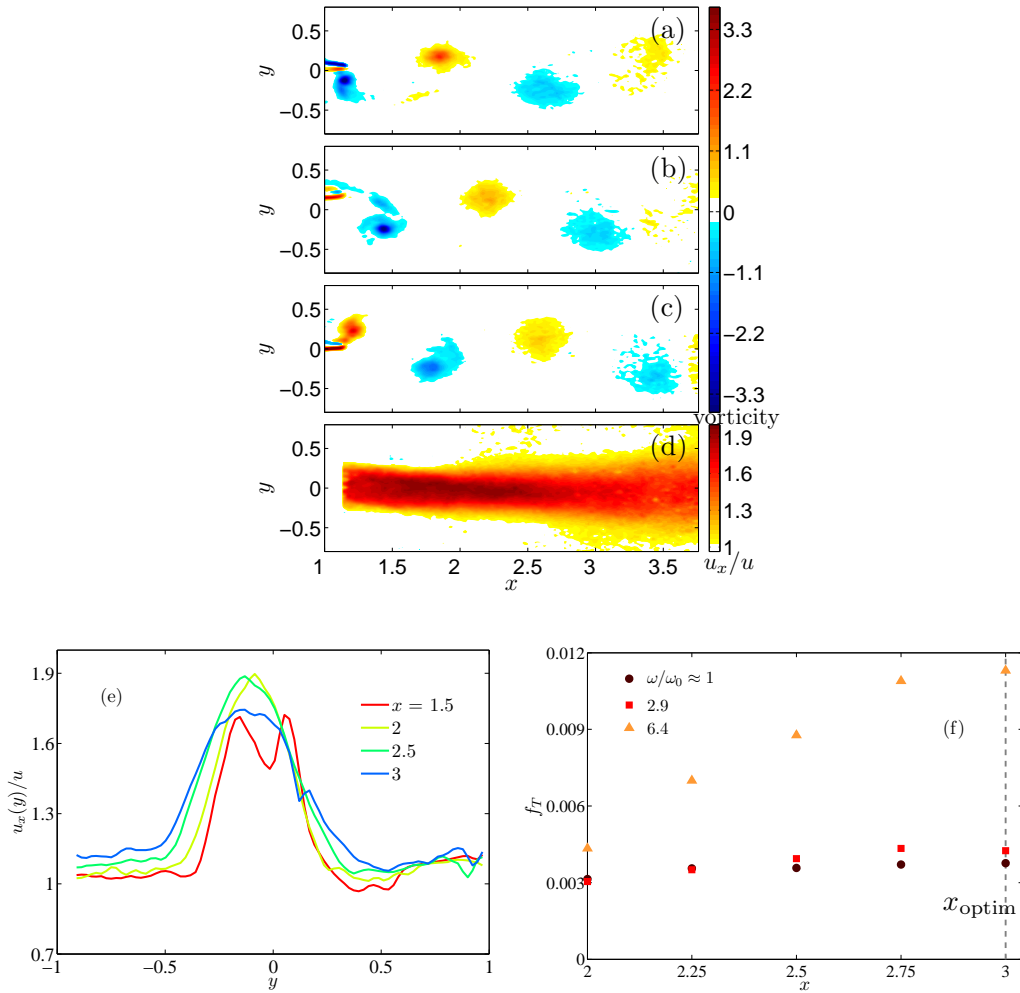


FIG. 7. Phase-averaged vorticity field in the wake of the heaving flexible foil for $\omega t = \pi/2$ (a) π (b), and $3\pi/2$ (c). Flow speed is $u = 0.049$ and plate bending rigidity $B = 0.027$ Nm. The foil is forced at amplitude $a_{\text{LE}} = 0.07$ and frequency $\omega = \omega_0$. (d) Time-averaged x -component of the flow velocity, u_x , relative to the imposed flow speed u for the same parameters. (e) Mean velocity profile $u_x(y)$ for different distances x behind the moving plate for the same parameters. (f) Thrust f_T calculated from (6) for several forcing frequencies ω/ω_0 as a function of the position x behind the plate. The evolution of f_T reveals an optimal distance x_{optim} . (for which $\partial_x f_T = 0$), which varies from 2.5 to 3 depending on the forcing frequency.

The expression of the total thrust can be written $f_T = f_P + f_R$, with

$$f_P = -\frac{1}{2} \Re \int_{-1}^1 p \overline{\partial_x h} dx, \quad (7)$$

$$f_R = -\frac{1}{2} \Re \int_{-1}^1 \left(m\nu \partial_t h + \frac{4}{3\pi} c_D |\partial_t h| \partial_t h \right) \overline{\partial_x h} dx, \quad (8)$$

where \Re stands for the real part and the overbar for the complex conjugate. For more details on these calculations, see Appendix A and Refs. 19,21, and 41. It can be seen that, when nonlinear terms are neglected, the thrust is quadratic in amplitude, as expected. It is also proportional to the square of the forcing frequency. It is thus expected that the

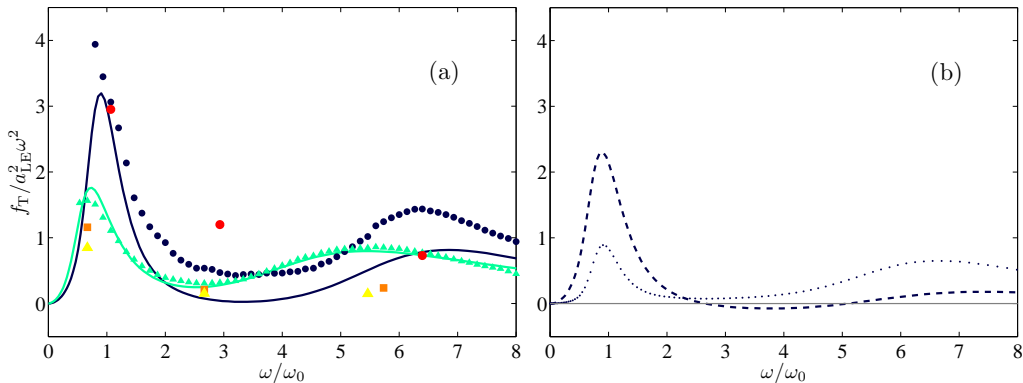


FIG. 8. (a) Comparison of the thrust calculated in the model (lines) and experimental measurements (symbols). Dark blue (circles) and light green (triangles) correspond respectively to the forcing amplitude $a_{LE} = 0.07$ and 0.24 , with the plate rigidity $B = 0.027$ Nm placed in water at rest. Close-by symbols are obtained with load cells, while red and yellow symbols are obtained from PIV and the momentum balance in Eq. (6) for $u = 0.049$. (b) Different contributions of the total thrust for $a_{LE} = 0.07$: reactive forces (dashed line) and resistive forces (dotted line).

dimensionless thrust will scale as $f_T = O(a_{LE}^2 \omega^2)$, which corresponds to a dimensioned thrust scaling as $F_T = O(\rho U_{LE}^2 C)$, where $U_{LE} = \Omega A_{LE}$ is the typical velocity of the leading edge.

In Fig. 8a, the total thrust f_T calculated with this method is compared to experimental measurements. Despite some differences for the smallest forcing amplitude which are likely due to the hypothesis of zero leading edge suction, the average thrust generated is well predicted. In particular, the nonlinearities, which explain the differences between the two sets of data of different forcing amplitudes, are well reproduced around $\omega / \omega_0 = 1$. In Fig. 8a, the thrust measured from the momentum balance equation (6) is shown together with the average thrust recorded by the load cells. These measurements are consistent for low frequencies ($\omega / \omega_0 \approx 1$), however thrust calculated from PIV data is only a raw approximation for $\omega / \omega_0 > 2$. This is likely due to the three-dimensionality of the flow.

These experimental results confirm the work of Michelin *et al.*³⁴: resonances in thrust appears at the same frequencies as resonances in amplitude. Indeed, the maximum of thrust, $f_T / (a_{LE}^2 \omega^2)$, occurs at $\omega / \omega_0 = 0.9$ for the forcing amplitude $a_{LE} = 0.07$ (dark blue in Fig. 8a) and $\omega / \omega_0 = 0.7$ for the forcing amplitude $a_{LE} = 0.24$ (light green in Fig. 8a).

As mentioned above Eq. (7), if leading edge suction f_S is neglected, the total thrust can be split up into two contributions: resistive forces f_R and reactive forces f_P (Fig. 8b). Around the first resonance and for small forcing amplitude, f_P dominates (it is 2.3 times larger than f_R at $\omega / \omega_0 = 0.9$). But in all other cases (large forcing amplitude or $\omega / \omega_0 > 1$), the resistive contribution is of same order, if not larger than f_P . In the interval $2.7 \leq \omega / \omega_0 \leq 5.1$, f_P can even be negative; in this interval, the total thrust is positive only thanks to resistive forces.

C. Efficiency

Let us now address the question of efficiency of thrust generation. For simplicity, we will make additional assumptions in this section: the foil will be considered near its first resonance (such that its deformation can be represented by the first beam eigenmode only), and linear damping terms will be neglected. However, we will lift the hypothesis

of large reduced frequency k . With these assumptions Eq. (4) becomes

$$\kappa_1^4 a + \frac{u^2 c_D a_{LE}}{m} \frac{2}{3\pi} \int_{-1}^1 h_1 |ik(1 + ah_1) + a\partial_x h_1| (ik(1 + ah_1) + a\partial_x h_1) dx - \frac{u^2}{m} (b_0(k) + b_1(k)a) = 0, \quad (9)$$

with $a = a_1/a_{LE}$, $h(x, t) = a_{LE}(1 + ah_1(x))e^{i\omega t}$, and

$$b_0(k) \approx 1.188k^2 - 0.995ikC_{Th}(k), \quad (10)$$

$$b_1(k) \approx 1.131k^2 - 2.216ik - 0.261 - (1.247 + 1.350ik)C_{Th}(k), \quad (11)$$

where $C_{Th}(k)$ is the Theodorsen function⁵⁴

$$C_{Th}(k) = \frac{H_1^{(2)}(k)}{H_1^{(2)}(k) + iH_0^{(2)}(k)}, \quad (12)$$

with $H_n^{(2)}$ the Hankel function of the second kind. In Eq. (9), we recognize the elastic, nonlinear damping, and pressure terms respectively. In Eqs. (10–11), the first terms corresponds to β_{10} and β_{11} in Eq. (4), as given in Table II, and the other terms arise because we are no longer in the limit of asymptotically large k .

The average power needed to actuate the foil can be split into a reactive and a resistive components: $\varpi = \varpi_P + \varpi_R$, with

$$\varpi_P = \frac{1}{2\omega} \int_{-1}^1 \Re(p \overline{\partial_t h}) dx, \quad (13)$$

$$\varpi_R = \frac{1}{2\omega} \int_{-1}^1 \frac{4}{3\pi} c_D \Re[|\partial_t h + u\partial_x h| (\partial_t h + u\partial_x h) \overline{\partial_t h}] dx. \quad (14)$$

The dimensionless power ϖ is related to the dimensioned average power per unit span through the relation $\mathcal{P} = \rho B \Omega \varpi / M$ (in W m^{-1}). From the power ϖ and the thrust f_T , the Froude efficiency η can be defined

$$\eta = \frac{F_T U}{\mathcal{P}} = \frac{f_T}{k\varpi}. \quad (15)$$

Because our set-up does not allow us to measure the energy given to the system, we are going to use the experimental data of Quinn *et al.*³⁰ to assess the validity of these theoretical predictions on power cost and efficiency. Their set-up is very similar to the one used here, but the linear damping of their plates was not quantified and will be neglected here. We will also assume that the drag coefficient is the same as in the present study: $c_D = 12$. Figure 9 shows how the trailing edge deflection amplitude, the thrust produced, the average power needed, and the Froude efficiency vary as a function of the forcing frequency when the forcing amplitude and flow velocity are fixed (frequency response test). Similarly to the results of the present study, these plots exhibit a maximum around the resonance $\omega \approx \omega_0$. Although we use the same value as in our study for the fitting parameters c_D , all quantities are well predicted by the model, except the thrust and power that are slightly over-predicted. This may be because linear damping terms have been neglected.

Using Froude efficiency to measure the performance of thrust generation has been criticized by some authors (e.g., Refs. 55 and 56). These critics point out that Froude efficiency does not allow to compare fairly different propulsion systems. Here, we propose a different approach: we will formulate and solve an optimization problem with the

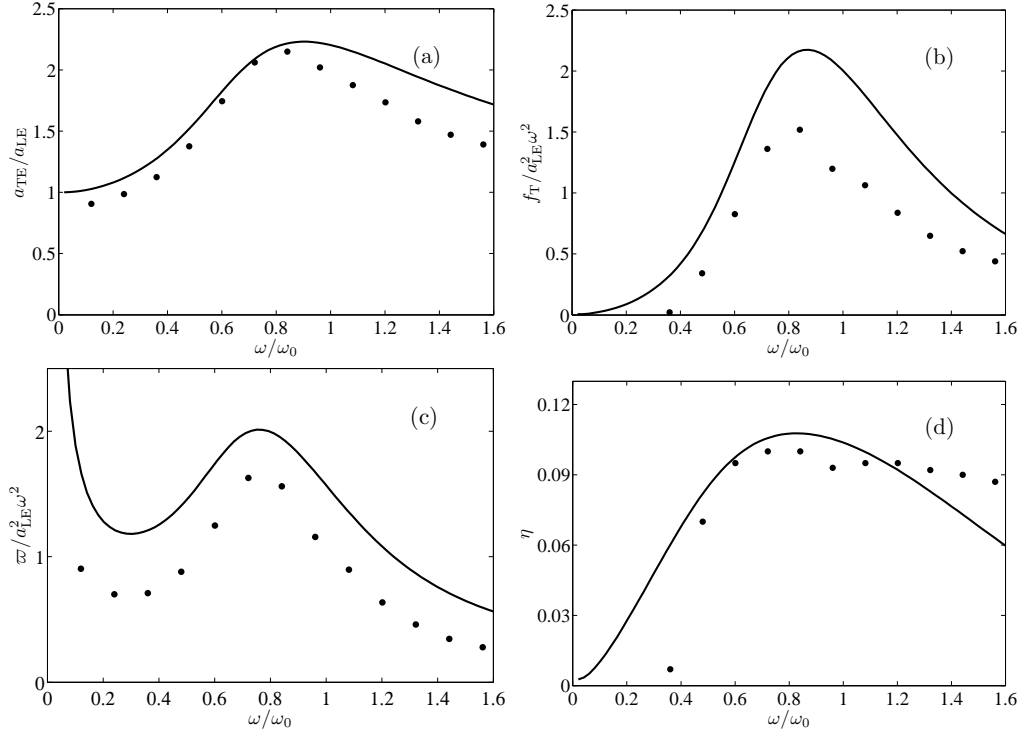


FIG. 9. Experimental data from Quinn *et al.*³⁰ compared to the presented model: (a) amplitude response; (b) thrust generated; (c) power cost; and (d) Froude efficiency for $a_{LE} \approx 0.1$ and $u = 0.016$.

constraint of constant thrust. Within this framework, the Froude efficiency η is a natural measure of optimality (although, arguably, other choices would be equivalent).

Let us assume we want to design an optimal propeller for a given vessel at a given traveling speed. In dimensioned units, we thus consider that the speed U , the fluid density ρ , the foil surface density M , the foil half-chord C , and the desired average thrust F_T are known. On the other hand, the foil bending rigidity B , actuating frequency Ω and amplitude A_{LE} have to be chosen such that the average power needed \mathcal{P} is minimal.

The five given variables can be expressed with three independent units, such that two dimensionless numbers can be built: the mass ratio, $m = M/\rho C$, and the Lighthill number²⁵, $Li = F_T/(\rho U^2 C) = f_T/u^2$. We will assume that m is asymptotically small, which justifies a posteriori to neglect inertial and linear damping terms in (9). The Lighthill number can be seen as the ratio between the desirable thrust, or the drag that needs to be balanced, and a typical achievable thrust (per unit span): $\rho U^2 C$. The three design parameters B , Ω , and A_{LE} correspond in dimensionless units to rigidity $b = B/(\rho U^2 C^3) = m/u^2$, reduced frequency $k = \Omega C/U$, and forcing amplitude $a_{LE} = A_{LE}/C$ respectively. Note that, in Eq. (9), u always appears as u^2/m , which is the reason why b is used as a parameter instead of u .

The constrained optimization problem we want to solve consists in finding

$$\max \eta \quad \text{such that} \quad \begin{cases} f_T = Li u^2, \\ (b, k, a_{LE}) \in \mathbb{R}^3. \end{cases} \quad (16)$$

To perform this optimization, we first fix the value of Li and assume a certain value for b . Then, for each value of the reduced frequency k , we calculate the amplitude a_{LE} needed to generate a thrust $f_T = Li u^2$, and the corresponding efficiency η . To perform

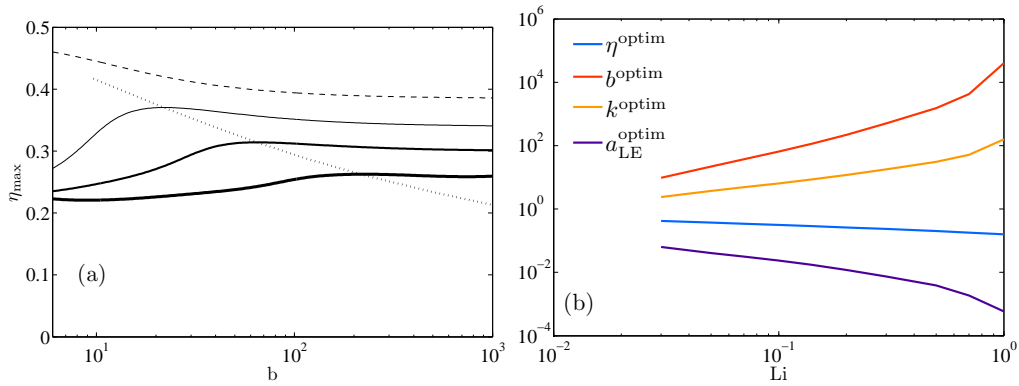


FIG. 10. Optimal heaving of a flexible plate: (a) η_{\max} as a function of the rigidity b for four values of Li : 0.02 (dashed line), 0.05 (thin line), 0.1 (medium), 0.2 (thick). The dotted line shows the loci of the optimal values η^{optim} for $Li \geq 0.03$. (b) Optimal value of the efficiency η^{optim} , and corresponding values of the rigidity b^{optim} , reduced frequency k^{optim} , and forcing amplitude $a_{\text{LE}}^{\text{optim}}$, as a function of Li .

this calculation of the thrust f_T , we do not neglect the leading-edge suction anymore (cf. Appendix C). For a certain frequency k , the efficiency reaches a maximum value $\eta_{\max}(Li, b)$. We then repeat this operation for different values of the rigidity b to identify the maximum of η_{\max} (Fig. 10a). This maximum actually corresponds to the optimal value η^{optim} associated to a triplet $(b^{\text{optim}}, k^{\text{optim}}, a_{\text{LE}}^{\text{optim}})$. Figure 10b shows how the value of these parameters vary as a function of the Lighthill number in the range $0.03 \leq Li \leq 1$. For small thrust values, the optimum is achieved by a highly flexible foil flapping relatively slowly at large amplitude. Meanwhile, for higher thrusts, stiffer foils flapping rapidly at small amplitudes are preferable.

For smaller Lighthill numbers ($Li \leq 0.02$), the optimum is reached in the limit of vanishing rigidity b . In that case, the optimum motion corresponds to an infinite forcing amplitude a_{LE} , but finite leading edge speed ka_{LE} . This shows the limits of the present approach. For large forcing amplitude, the weakly nonlinear approximation is not valid and, in any case, the results of the present optimization calculation are quite sensitive to the way the leading edge suction and separation are modeled (Appendix C).

Nevertheless, Figure 10 shows that, for moderate values of the Lighthill number, an optimal spot exists in the parameter space. This optimal motion always corresponds to a resonance of the flapping plate: for $0.03 \leq Li \leq 1$, the frequency is always in the narrow range $1.03 \leq \omega/\omega_0 \leq 1.07$ corresponding to the resonance of the first eigenmode. However, the optimal flapping amplitude does not correspond to a quasi constant Strouhal number, contrarily to what has been recently suggested²⁶. In the range where an optimal motion exists ($0.03 \leq Li \leq 1$), the Strouhal number of the optimal flapping behaves as $St^{\text{optim}} \approx 0.5 Li^{0.5}$, thus varying between 0.08 and 0.5 in the interval considered. Here the Strouhal number is constructed with the amplitude of the trailing edge deflection: $St = \Omega A_{\text{TE}}/(\pi U) = ka_{\text{TE}}/\pi$. This can be compared to the scaling found in the limit of elongated bodies²⁵, where it was also found that Strouhal number is not constant for the optimal motion: $St^{\text{optim}} \approx 0.75 Li^{0.33}$ (note that the definition of the Lighthill number was slightly different in this previous study because the problem considered was three-dimensional).

To get an estimate of the Lighthill number for a fish, or a bio-inspired swimming vessel, we can assume that the propeller half-chord C and half-span S are equal and that the aspect ratio of the whole swimmer is $1/5$: $C = 0.1L$, where L is the total swimmer's length. If most of the drag is due to skin friction, the thrust needed to balance this drag (per unit

span) is approximately $F_T \approx \frac{1}{2}\rho U^2 \text{Re}^{-1/2} L^2 / C$ when the boundary layers are laminar, with the Reynolds number based on the length, $\text{Re} = UL/\nu$. The resulting Lighthill number is thus $\text{Li} = F_T / (\rho U^2 C) \approx 50 \text{Re}^{-1/2}$. This Lighthill number corresponds to $\text{St}^{\text{optim}} \approx 3.5 \text{Re}^{-1/4}$, which is roughly the scaling found in a recent compilation of biological data⁵⁷ for laminar boundary layers, i.e. $\text{Re} \lesssim 10^5$. Note however that the Strouhal number may not be a good measure of optimality, as it can simply be seen as the result from a balance of thrust and drag for a specific swimming speed.

V. DISCUSSION

In summary, we have studied the kinematic and dynamic response of a flexible foil actuated in heave at its leading edge. This experimental investigation has been performed on a forcing frequency range including the two first resonances of the foil+fluid system. It was found that the forcing amplitude is an important parameter to predict the response, or, in other words, that nonlinearities are crucial even for relatively small deflections. Based on this observation, a weakly nonlinear, two-dimensional, and inviscid model has been developed. In this model, nonlinearities arise from a transverse drag force, which acts as a quadratic damping (nonlinear cubic terms being neglected). The magnitude of this drag, which is varied through a drag coefficient, is a free parameter of the model that is adjusted to fit the frequency responses tests performed at different forcing amplitudes. Once this adjusting parameter is set, agreement between experimental observations and model predictions is good for the first two resonances, at all amplitudes tested.

With the same model, the average thrust generated by the foil and the average power spent for actuation can also be calculated. There is a good agreement between the predictions of these quantities and the data of the present study, as well as the data of Quinn *et al.*³⁰ who used a similar set-up. From the power and thrust, a Froude efficiency can be defined. We have shown that this definition of efficiency is a natural choice to solve the following optimization problem: given a certain thrust to be produced and a given swimming velocity, what is the best design choice for the flexible propeller, i.e. the choice of rigidity, forcing amplitude, and forcing frequency that minimize the power needed? Within the framework of the proposed model, we have solved this optimization problem and have shown that optimal motions always correspond to resonances of the foil+fluid system. However, contrarily to recent findings²⁶, the overall optimum is not achieved for a quasi constant Strouhal number.

The proposed model has some drawbacks however that should be addressed in the future if one wants to really design an optimal bio-inspired propeller. First, nonlinearities should be taken into account more rigorously, maybe through numerical simulations. Then, the two-dimensional hypothesis should be lifted to account for moderate aspect ratios such as those encountered in nature. Finally, when the thrust force is relatively large (i.e. for large Lighthill numbers), the propeller kinematics cannot be fully dissociated from the bluff body that needs to be propelled. The flexible foil produced recoil torques on the body that induce a pitch rotation that needs to be taken into account. One possible avenue would be to use experimental optimization to find the best design choice⁵⁸. However, one has to be careful in defining the objective function and the constraints. We showed here that Froude efficiency can be meaningful when comparing propeller generating the *same* thrust force for the *same* swimming velocity.

ACKNOWLEDGMENTS

We warmly thank D. Quinn and A. Smits (Princeton University) for sending us their experimental data. We also thank both reviewers for their insightful comments on this work.

Appendix A: Amplitude equations

The modes $h_i(x)$ are found by calculating the eigenmodes of the linearized Euler–Bernoulli beam equation in vacuum, with clamped-free boundary conditions. They are given by⁵⁹

$$h_i(x) = \cosh \kappa_i(x+1) + \cos \kappa_i(x+1) + \zeta_i(\sinh \kappa_i(x+1) - \sin \kappa_i(x+1)), \quad (\text{A1})$$

with

$$\zeta_i = \frac{\sin(2\kappa_i) - \sinh(2\kappa_i)}{\cos(2\kappa_i) + \cosh(2\kappa_i)}, \quad (\text{A2})$$

where the wavenumbers κ_i are given in Table II for the first three eigenmodes.

To calculate the pressure jump across the foil, we will use a method first derived by Wu¹⁹. The only difference is that we will make the additional simplifying assumption that the reduced frequency is asymptotically large, i.e. $k \gg 1$. Since the potential problem is linear and we consider a perturbation of the uniform velocity field u , to each beam eigenmode $h_i(x)$ corresponds a pressure jump perturbation $p_i(x)$ at leading order.

Each eigenmode $h_i(x)$ is decomposed onto the Chebyshev functions of the first kind (i.e. $T_q(\cos \theta) = \cos(q\theta)$)

$$h_i(x) = \frac{1}{2}\xi_{1,1} + \sum_{q=2}^Q \xi_{1,q} T_{q-1}(x), \quad (\text{A3})$$

where

$$\xi_{iq} = \frac{2}{\pi} \int_0^\pi h_i(\cos \theta) \cos(q-1)\theta \, d\theta. \quad (\text{A4})$$

To find the acceleration potential $\varphi_i(x, y)e^{i\omega t}$ associated to each eigenmode of the plate $h_i(x)e^{i\omega t}$, one needs to solve a Laplace problem with a Neumann boundary condition (due to the impermeability of the plate)

$$\Delta \varphi_i = 0, \quad (\text{A5})$$

$$\frac{\partial \varphi_i}{\partial y} = -\omega^2 h_i(x), \quad \text{on } y = 0 \quad (-1 < x < 1), \quad (\text{A6})$$

in the limit of large ω . As explained by Wu¹⁹, the solution of this Laplace equation has been obtained by Küssner and Schwarz⁶⁰. The corresponding pressure jump (factorized by $-\omega^2$) is

$$p_i(\cos \theta) = \frac{1}{-\omega^2} [\varphi_i(\cos \theta, 0^-) - \varphi_i(\cos \theta, 0^+)] = \sum_{q=1}^Q \frac{\xi_{i(q+2)} - \xi_{iq}}{q} \sin q\theta, \quad (\text{A7})$$

where, in practice, we use $Q = 10$. Note that the numbers of Chebyshev functions Q is independent of the number of eigenmodes N . The total pressure jump is then simply

$$p(x) = -\omega^2 \left(a_{\text{LE}} p_{\text{LE}}(x) + \sum_{i=1}^N a_i p_i(x) \right), \quad (\text{A8})$$

where p_{LE} is the pressure associated to the heave of a rigid foil

$$p_{\text{LE}}(x) = -2\sqrt{1-x^2}. \quad (\text{A9})$$

The amplitude equations are obtained by first inserting the decomposition (2) into (1), and then by taking the scalar product [defined by (3)] with the N eigenmodes $h_i(x)$. This yields Eq. (4) where the coefficients α_i and β_{ij} are given by

$$\alpha_i = \langle h_i, 1 \rangle, \quad (\text{A10})$$

$$\beta_{i0} = \langle h_i, p_{LE} \rangle, \quad (\text{A11})$$

$$\beta_{ij} = \langle h_i, p_j \rangle, \quad (\text{A12})$$

for i and j between 1 and N .

Appendix B: Damping model

Impulse response tests in water and air have revealed the importance of damping in the system. If the initial deflection amplitude is small, two linear damping terms can be considered: linear fluid damping of coefficient ν and internal Kelvin–Voigt viscoelastic damping⁶¹ of coefficient μ (in dimensionless units).

During impulse response tests, we can assume that only the first eigenmode is present. The deflection of the plate is thus of the form

$$h(x, t) = \frac{1}{2} a_{\text{TE}}(t) h_1(x), \quad (\text{B1})$$

where the time-varying amplitude is a damped oscillation of the form

$$a_{\text{TE}}(t) = e^{i\omega_0 t} e^{-\sigma t}. \quad (\text{B2})$$

The form of ω_0 and σ is found by using the linearized Euler–Bernoulli equation (1) and neglecting the nonlinear damping term. In the limit of small damping, it is found that

$$\omega_0 \approx \frac{\kappa_1^2}{\sqrt{1 + \beta_{11}/m}}, \quad \text{and} \quad \sigma = -\frac{\nu + \mu\kappa_1^4}{2(1 + \beta_{11}/m)}. \quad (\text{B3})$$

From an experimental point of view, the natural frequency of the system, $\Omega_0 = (\omega_0/C^2)\sqrt{B/M}$, is measured by performing a Fourier transform of the damped oscillating signal. The damping coefficient $\Sigma = (\sigma/C^2)\sqrt{B/M}$ is measured by plotting in log-linear plot the amplitude of the trailing edge deflection as a function of time (inset of Fig. 2). In dimensional units, the damping coefficient Σ is related to the coefficient ν^* and μ^* through

$$2(1 + \beta_{11}/m)\Sigma = -\frac{1}{M} \left(\nu^* + \frac{\kappa_1^4}{C^4} \mu^* \right) \quad (\text{B4})$$

where ν^* and μ^* are the dimensional equivalents of ν and μ given by

$$\nu = \frac{\nu^* C^2}{\sqrt{MB}}, \quad \mu = \frac{\mu^*}{C^2 \sqrt{MB}} \quad (\text{B5})$$

In Figure 11, $2M(1 + \beta_{11}/m)|\Sigma|$ is plotted as a function of κ_1^4/C^4 for different impulse response tests performed in water (for a single value of C) and air (for different half-chords C). From the data in air and using the relation (B4), the viscoelastic coefficient μ^* can be measured: $\mu^* = 1.02 \times 10^{-6}$ N m s. From the data in water, the linear fluid damping coefficient can be measured: $\nu^* = 47.64$ kg m⁻² s⁻¹. Using the dimensionless forms of these coefficient with Eqs. (B5), it is found that $\nu = 0.583$ and $\mu = 9.64 \times 10^{-4}$ for experiments conducted in water with $C = 0.06$ m. Note that the linear fluid dissipation varies, the mean value is taken into the model is $\nu = 0.474$.

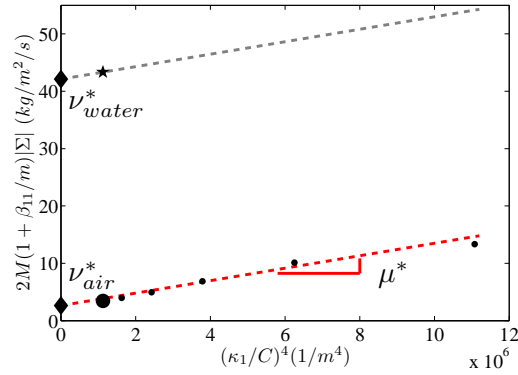


FIG. 11. Damping coefficient of a plate as a function of $(\kappa_1/C)^4$. Circles are the experimental data in air. A linear fit of these data yields the viscoelastic damping coefficient μ^* . The star represents the measured damping in water. The intersect between the linear fit of slope μ^* and the vertical axis gives the viscous damping coefficient ν^* , either in air or in water.

In addition to the linear fluid damping, the resistance to the transverse motion of the plate is expressed through a nonlinear drag force, with a drag coefficient c_D . From the literature^{45–47}, a classic value for a flat plate perpendicular to the flow is around 2 in the range of the Reynolds number tested. In the present case however, the plate is confined between walls, a configuration that probably affects the value of c_D . Moreover, nonlinear effects of order $O(a_{LE}^3)$ have been neglected in the analysis, but can be taken into account approximatively by including them in an “effective” drag coefficient. The value $c_D = 12$ seems to fully capture the frequency response tests performed (cf. Fig. 4). This unusually large value indicates that additional nonlinear effects should probably be taken into account in the model, in particular for the largest forcing amplitudes.

Appendix C: Leading-edge suction

As discussed in Sec. IV B, a thrust force arises from leading-edge suction when the angle of attack at the leading edge is non zero^{18–20,41}. From a mathematical point of view, this force can directly be linked to the intensity of the inverse square root singularity of the pressure jump at the leading edge.

When this force is considered, the total thrust can be written as $f_T = f_P + f_R + f_S$, with the reactive force f_P given by (7), the resistive force f_R given by (8), and the leading-edge suction f_S given by

$$f_S = g_S(ka_{LE}) \frac{\pi}{4} a_{LE}^2 \omega^2 |\gamma_{LE} + a\gamma_1|^2, \quad (C1)$$

where

$$\gamma_{LE} = -2ikC_{Th}(k), \quad (C2)$$

$$\gamma_1 = 1.040ik + 0.665 - (2.507 + 2.713ik)C_{Th}(k). \quad (C3)$$

The coefficients γ_{LE} and γ_1 are related to the intensity of the leading-edge singularity [in Ref. 19, these coefficients correspond to the coefficient a_0 given by Eq. (26b)].

The function $g_S(x)$ in (C1) is an ad hoc function, which decreases monotonically between 1 and 0

$$g_S(x) = \frac{1 - \tanh(15x - 3)}{2}, \quad (C4)$$

such that $g_S(0.2) = 0.5$. It crudely models the fact that the theoretical leading edge suction calculated with linear potential theory cannot be achieved when the angle of attack is too large because of separation. Here, the maximal value of the angle of attack is $\arctan(ka_{LE})$ and thus, we assume that leading-edge suction is decreased by a factor of 2 when the maximum angle of attack is equal to $\arctan(0.2) = 11.3^\circ$ and by a factor of 8.7 for maximum angle of attack of 15° . The fact that separation occurs around 15° has been shown experimentally¹⁸ and numerically⁶², although the precise form of the function g_S remains to be determined. It should be noted that the results of the optimization calculation performed in Sec. IV C can be quite sensitive to the way leading-edge suction and separation are modeled. This is because this force, which always contributes to a positive thrust, can take a large part in the production of thrust.

- ¹R. W. Blake, "Fish functional design and swimming performance," *J. Fish Biol.* **65**, 1193–1222 (2004), ISSN 1095-8649.
- ²R. Bainbridge, "Caudal fin and body movement in the propulsion of some fish," *J. Exp. Biol.* **40**, 23–56 (1963).
- ³F. E. Fish and G. V. Lauder, "Passive and active flow control by swimming fishes and mammals," *Ann. Rev. Fluid Mech.* **38**, 194–224 (2006).
- ⁴K. N. Lucas, N. Johnson, W. T. Beaulieu, E. Cathcart, G. Tirrell, S. P. Colin, B. J. Gemmel, J. O. Dabiri, and J. H. Costello, "Bending rules for animal propulsion," *Nat. Commun.* **5**, 3293 (2014).
- ⁵J. Katz and D. Weihs, "Hydrodynamic propulsion by large amplitude oscillation of an airfoil with chordwise flexibility," *J. Fluid Mech.* **88**, 485–497 (1978).
- ⁶S. Heathcote and I. Gursul, "Flexible flapping airfoil propulsion at low reynolds number," *AIAA J.* **45(5)**, 1066–1079 (2007).
- ⁷C. Marais, B. Thiria, J. E. Wesfreid, and R. Godoy-Diana, "Stabilizing effect of flexibility in the wake of a flapping foil," *J. Fluid Mech.* **710**, 659 (2012).
- ⁸J. R. Nursall, "The caudal fin as a hydrofoil," *Evolution* **12**, 116–120 (1958).
- ⁹C. W. McCutchen, "The trout tail fin: a self-cambering hydrofoil," *J. Biomech.* **3**, 271–281 (1970).
- ¹⁰J. Gray, "Studies in animal locomotion. I. The movement of fish with special reference to the eel," *J. Exp. Biol.* **10**, 88–104 (1933).
- ¹¹J. Gray, "Studies in animal locomotion: VI. The propulsive powers of the dolphin," *J. Exp. Biol.* **13**, 192–199 (1936).
- ¹²R. Bainbridge, "The speed of swimming of fish as related to size and to frequency and amplitude of the tail beat," *J. Exp. Biol.* **35**, 109–133 (1958).
- ¹³C. C. Lindsey, "Form, function and locomotory habits in fish," in *Fish Physiology VII*, edited by W. S. Hoar and D. J. Randall (Academic Press, 1978) pp. 1–100.
- ¹⁴G. V. Lauder and E. D. Tytell, "Hydrodynamics of undulatory propulsion," *Fish Physiol.* **23**, 425–468 (2005).
- ¹⁵M. S. Triantafyllou and G. S. Triantafyllou, "An efficient swimming machine," *Sci. Am.* **272**, 64–71 (1995).
- ¹⁶M. Koochesfahani, "Vortical patterns in the wake of an oscillating airfoil," *AIAA J.* **27**, 1200–1205 (1989).
- ¹⁷G. S. Triantafyllou, M. S. Triantafyllou, and M. A. Grosenbaugh, "Optimal thrust development in oscillating foils with application to fish propulsion," *J. Fluids Struct.* **7**, 205–224 (1993).
- ¹⁸L. Schouveiler, F. S. Hover, and M. S. Triantafyllou, "Performance of flapping foil propulsion," *J. Fluids Struct.* **20**, 949–959 (2005).
- ¹⁹T. Y.-T. Wu, "Swimming of a waving plate," *J. Fluid Mech.* **10**, 321–344 (1961).
- ²⁰M. J. Lighthill, "Aquatic animal propulsion of high hydromechanical efficiency," *J. Fluid Mech.* **44**, 265–301 (1960).
- ²¹T. Y.-T. Wu, "Hydrodynamics of swimming propulsion. part 2. some optimum shape problems," *J. Fluid Mech.* **46**, 521–544 (1971).
- ²²J. M. Anderson, K. Streitlien, D. S. Barrett, and M. S. Triantafyllou, "Oscillating foils of high propulsive efficiency," *J. Fluid Mech.* **360**, 41–72 (4 1998).
- ²³D. A. Read, F. S. Hover, and M. S. Triantafyllou, "Forces on oscillating foils for propulsion and maneuvering," *J. Fluids Struct.* **17**, 163–183 (2003).
- ²⁴G. K. Taylor, R. L. Nudds, and A. L. R. Thomas, "Flying and swimming animals cruise at a Strouhal number tuned for high power efficiency," *Flying and swimming animals cruise at a Strouhal number tuned for high power efficiency*, *Nature* **425**, 707–711 (2003).
- ²⁵C. Eloy, "Optimal Strouhal number for swimming animals," *J. Fluids Struct.* **30**, 205–218 (2012).
- ²⁶P. A. Dewey, B. M. Boschitsch, K. W. Moored, H. A. Stone, and A. J. Smits, "Scaling laws for the thrust production of flexible pitching panels," *J. Fluid Mech.* **732**, 29–46 (10 2013).
- ²⁷K. W. Moored, P. A. Dewey, A. J. Smits, and H. Haj-Hariri, "Hydrodynamic wake resonance as an underlying principle of efficient unsteady propulsion," *J. Fluid Mech.* **708**, 329–348 (10 2012).

- ²⁸S. E. Spagnolie, L. Moret, M. J. Shelley, and J. Zhang, “Surprising behaviors in flapping locomotion with passive pitching,” *Phys. Fluids* **22**, 041903 (2010).
- ²⁹S. Alben, S. Witt, T. V. Baker, S. Anderson, and G. V. Lauder, “Dynamics of freely swimming flexible foils,” *Phys. Fluids* **24**, 051901 (2012).
- ³⁰D. B. Quinn, G. V. Lauder, and A. J. Smits, “Scaling the propulsive performance of heaving flexible panels,” *J. Fluid Mech.* **738**, 250–267 (2014).
- ³¹F. Paraz, C. Eloy, and L. Schouveiler, “Experimental study of the response of a flexible plate to a harmonic forcing in a flow,” *C.R. Mécanique* **342**, 532–538 (2014).
- ³²C. J. Esposito, J. L. Tangorra, B. E. Flammang, and G. V. Lauder, “A robotic fish caudal fin: effects of stiffness and motor program on locomotor performance,” *J. Exp. Biol.* **215**, 56–67 (2012).
- ³³A.J. Richards and P. Oshkai, “Effect of the stiffness, inertia and oscillation kinematics on the thrust generation and efficiency of an oscillating-foil propulsion system,” *J. Fluids Struct.* **57**, 357–374 (2015).
- ³⁴S. Michelin and S. G. Llewellyn Smith, “Resonance and propulsion performance of a heaving wing,” *Phys. Fluids* **21**(7), 071902 (2009).
- ³⁵J. D. Eldredge, J. Toomey, and A. Medina, “On the roles of chord-wise flexibility in a flapping wing with hovering kinematics,” *J. Fluid Mech.* **659**, 94–115 (2010).
- ³⁶C.-K. Kang, H. Aono, C.E.C Cesnik, and W. Shyy, “Effect of flexibility on the aerodynamic performance of flapping wings,” *J. Fluid Mech.* **689**, 32–74 (2011).
- ³⁷P. J. S. A. Ferreira de Sousa and J. J. Allen, “Thrust efficiency of harmonically oscillating flexible flat plates,” *J. Fluid Mech.* **674**, 43–66 (2011).
- ³⁸R.-N. Hua, L. Zhu, and X.-Y. Lu, “Locomotion of a flapping flexible plate,” *Phys. Fluids* **25**, 121901 (2013).
- ³⁹M. Bergmann, A. Iollo, and R. Mittal, “Effect of caudal fin flexibility on the propulsive efficiency of a fish-like swimmer,” *Bioinspir. Biomim.* **9**, 046001 (2014).
- ⁴⁰M. N. J. Moore, “Analytical results on the role of flexibility in flapping propulsion,” *J. Fluid Mech.* **757**, 599–612 (2014).
- ⁴¹C. Eloy and L. Schouveiler, “Optimisation of two-dimensional undulatory swimming at high Reynolds number,” *Int. J. Nonlinear Mech.* **46**, 568–576 (2011).
- ⁴²P. Meunier and T. Leweke, “Analysis and treatment of errors due to high velocity gradients in particle image velocimetry,” *Exp. Fluids* **35**, 408–421 (2003), ISSN 0723-4864.
- ⁴³D. G. Crighton, “The Kutta condition in unsteady flow,” *Ann. Rev. Fluid Mech.* **17**, 411–445 (1985).
- ⁴⁴C. Eloy, N. Kofman, and L. Schouveiler, “The origin of hysteresis in the flag instability,” *J. Fluid Mech.* **691**, 583–593 (2012).
- ⁴⁵S. F. Hoerner, *Fluid-dynamic drag: practical information on aerodynamic drag and hydrodynamic resistance* (Hoerner Fluid Dynamics, 1965).
- ⁴⁶M. Luhar and H.M. Nepf, “Flow-induced reconfiguration of buoyant and flexible aquatic vegetation,” *Limnol. Oceanogr.* **56**, 2003–2017 (6 2011).
- ⁴⁷P. Buchak, C. Eloy, and P. M. Reis, “The clapping book: Wind-driven oscillations in a stack of elastic sheets,” *Phys. Rev. Lett.* **105**, 194301 (2010).
- ⁴⁸A. Andersen, U. Pesavento, and Z.J. Wang, “Analysis of transitions between fluttering, tumbling and steady descent of falling cards,” *J. Fluid Mech.* **541**, 91–104 (10 2005), ISSN 1469-7645.
- ⁴⁹F. Paraz, C. Eloy, and L. Schouveiler, “Vortex patterns generated by a heaving flexible plate,” *J. Vis.* **17**, 295–297 (2014).
- ⁵⁰R. Godoy-Diana, J.L. Aider, and J.E. Wesfreid, “Transition in the wake of a flapping foil,” *Phys. Rev. E* **77**, 016308 (2008).
- ⁵¹G. K. Batchelor, *An introduction to fluid dynamics* (Cambridge University Press, 1967).
- ⁵²T. Von Kármán and J. M. Burgers, *General aerodynamic theory. Perfect fluids*, v. 2 (Springer, 1935).
- ⁵³C. Wang and J. D. Eldredge, “Low-order phenomenological modeling of leading-edge vortex formation,” *Theor. Comp. Fluid Dyn.* **27**, 577–598 (2013).
- ⁵⁴T. Theodorsen, “General theory of aerodynamic instability and the mechanism of flutter,” *Tech. Rep. TR-496* (NACA, 1935).
- ⁵⁵D. S. Barrett, M. S. Triantafyllou, D. K. P. Yue, M. A. Grosenbaugh, and M. J. Wolfgang, “Drag reduction in fish-like locomotion,” *J. Fluid Mech.* **392**, 183–212 (1999).
- ⁵⁶MS Triantafyllou, DKP Yue, and AP Maertens, “Efficiency of fish propulsion,” *Bioinspir. Biomim.* **10**, 46013–46023 (2015).
- ⁵⁷M. Gazzola, M. Argentina, and L. Mahadevan, “Scaling macroscopic aquatic locomotion,” *Nature Physics*, 758–761(2014).
- ⁵⁸D. B. Quinn, G. V. Lauder, and A. J. Smits, “Maximizing the efficiency of a flexible propulsor using experimental optimization,” *J. Fluid Mech.* **767**, 430–448 (2015).
- ⁵⁹L. D. Landau and E. M. Lifschitz, *Theory of elasticity* (Pergamon Press, New York, 1986).
- ⁶⁰H. G. Küssner and I. Schwarz, “The oscillating wing with aerodynamically balanced elevator,” *Tech. Rep. TM-991* (NACA, 1941).
- ⁶¹M. P. Paidoussis, “Fluid-structure interactions - slender structures and axial flow,” (Elsevier Academic Press, 2004).
- ⁶²M. H. Akbari and S. J. Price, “Simulation of dynamic stall for a NACA0012 airfoil using a vortex

method," *J. Fluids Struct.* **17**, 855–874 (2003).